Icarus 228 (2014) 364–374

Contents lists available at ScienceDirect

Icarus

journal homepage: www.elsevier.com/locate/icarus

The low-iron, reduced surface of Mercury as seen in spectral reflectance by MESSENGER

Noam R. Izenberg [a,*], Rachel L. Klima [a], Scott L. Murchie [a], David T. Blewett [a], Gregory M. Holsclaw [b], William E. McClintock [b], Erick Malaret [c], Calogero Mauceri [c], Faith Vilas [d], Ann L. Sprague [e], Jörn Helbert [f], Deborah L. Domingue [d], James W. Head III [g], Timothy A. Goudge [g], Sean C. Solomon [h,i], Charles A. Hibbitts [a], M. Darby Dyar [j]

[a] Planetary Exploration Group, The Johns Hopkins University Applied Physics Laboratory, Laurel, MD 20723, USA
[b] Laboratory for Atmospheric and Space Physics, University of Colorado, Boulder, CO 80303, USA
[c] Applied Coherent Technology Corporation, Herndon, VA 20170, USA
[d] Planetary Science Institute, Tucson, AZ 85719, USA
[e] Lunar and Planetary Laboratory, University of Arizona, Tucson, AZ 85721, USA
[f] Institute of Planetary Research, Deutsches Zentrum für Luft und Raumfahrt, D-12489 Berlin, Germany
[g] Department of Geological Sciences, Brown University, Providence, RI 02912, USA
[h] Department of Terrestrial Magnetism, Carnegie Institution of Washington, Washington, DC 20015, USA
[i] Lamont-Doherty Earth Observatory, Columbia University, Palisades, NY 10964, USA
[j] Department of Astronomy, Mount Holyoke College, South Hadley, MA 01075, USA

ARTICLE INFO

Article history:
Received 7 July 2013
Revised 19 October 2013
Accepted 20 October 2013
Available online 26 October 2013

Keywords:
Mercury
Mercury, surface
Spectroscopy

ABSTRACT

The MESSENGER spacecraft's Mercury Atmospheric and Surface Composition Spectrometer (MASCS) obtained more than 1.6 million reflectance spectra of Mercury's surface from near-ultraviolet to near-infrared wavelengths during the first year of orbital operations. A global analysis of spectra in the wavelength range 300–1450 nm shows little regional variation in absolute reflectance or spectral slopes and a lack of mineralogically diagnostic absorptions. In particular, reflectance spectra show no clear evidence for an absorption band centered near 1 μm that would be associated with the presence of ferrous iron in silicates. There is, however, evidence for an ultraviolet absorption possibly consistent with a very low iron content (2–3 wt% FeO or less) in surface silicates and for the presence of small amounts of metallic iron or other opaque minerals in the form of nano- or micrometer-sized particles. These findings are consistent with MESSENGER X-ray and gamma-ray measurements of Mercury's surface iron abundance. Although X-ray and gamma-ray observations indicate higher than expected quantities of sulfur on the surface, reflectance spectra show no absorption bands diagnostic of sulfide minerals. Whereas there is strong evidence of water ice in permanently shadowed craters near Mercury's poles, MASCS spectra provide no evidence for hydroxylated materials near permanently shadowed craters.

© 2013 Elsevier Inc. All rights reserved.

1. Introduction

The MErcury Surface, Space ENvironment, GEochemistry, and Ranging (MESSENGER) spacecraft (Solomon et al., 2007), in orbit about Mercury since March 2011, has shown that the surface of the innermost planet consists globally of a mix of smooth plains units and more heavily cratered areas. Most of the smooth plains are volcanic in origin, and areas of smooth plains constitute ~27% of the planet's surface (Denevi et al., 2013); the rest of the surface is dominated by older intercrater plains and heavily cratered terrain. The spectrum of Mercury's surface exhibits a "red" spectral slope, i.e., the reflectance increases with increasing wavelength. In comparison with the Moon, Mercury's spectral slope is generally steeper and the average reflectance is lower, suggesting some combination of more rapid optical maturation due to "space weathering" and a different average composition (e.g., Warell et al., 2006; Robinson et al., 2008; Holsclaw et al., 2010; Riner and Lucey, 2012). MESSENGER flyby data (McClintock et al., 2008) and ground-based visible, near-infrared, and mid-infrared spectra (Vilas, 1988; Sprague et al., 2002) suggest that Mercury's surface silicates are very low in iron, despite a planetary bulk density indicating that Mercury has a large, iron-rich core.

Since MESSENGER entered orbit about Mercury, X-Ray Spectrometer (XRS) measurements have revealed that the total surface

* Corresponding author. Address: Planetary Exploration Group, The Johns Hopkins University Applied Physics Laboratory, 11100 Johns Hopkins Road, Laurel, MD 20723, USA.
E-mail address: noam.izenberg@jhuapl.edu (N.R. Izenberg).

0019-1035/$ - see front matter © 2013 Elsevier Inc. All rights reserved.
http://dx.doi.org/10.1016/j.icarus.2013.10.023

abundance of Fe is low, with an upper limit of 4 wt%, and the Ti abundance is less than 0.8 wt% (Nittler et al., 2011). Data from the Gamma-Ray Spectrometer (GRS) (Evans et al., 2012) corroborate the low surface Fe abundance and indicate an average northern hemisphere value of 1.9 ± 0.3 wt%. In contrast, sulfur is unexpectedly abundant on Mercury's surface, with XRS and GRS measurements indicating a global range of ~1–4 wt% (Nittler et al., 2011; Weider et al., 2012) and a northern hemisphere average of 2.3 ± 0.4 wt% (Evans et al., 2012).

Multispectral imaging observations obtained with MESSENGER's Mercury Dual Imaging System (MDIS) (Hawkins et al., 2007) have enabled Mercury's surface to be divided into several terrain types on the basis of morphology, stratigraphy, and color variation (Robinson et al., 2008; Blewett et al., 2009; Denevi et al., 2009). The youngest widespread unit, smooth plains, can be further divided into high-reflectance red plains, intermediate plains, and low-reflectance blue plains (Denevi et al., 2009, 2013). Low-reflectance material (LRM) (Robinson et al., 2008), distinct from low-reflectance blue plains, is generally associated with material excavated by impact craters and basins. Also spectrally distinct are a number of smaller units, including bright material exposed by the youngest impact craters (Robinson et al., 2008); bright, relatively blue "hollows" (Blewett et al., 2011, 2013); and bright, relatively red pyroclastic deposits (e.g., Kerber et al., 2009, 2011; Goudge et al., 2012).

MESSENGER's Mercury Atmospheric and Surface Composition Spectrometer (MASCS) (McClintock and Lankton, 2007; McClintock et al., 2008) provides globally distributed measurements of spectral reflectance at a spectral resolution finer than and covering a greater wavelength range than the multispectral imaging of MDIS. In this paper we use orbital observations of Mercury's spectral reflectance obtained with the Visible and Infrared Spectrograph (VIRS) channel of MASCS to constrain the mineralogy of Mercury, including the materials and phases that might host the small amounts of iron detected at the surface. We also search for associations between spectral variations of surface materials and morphological units and geological processes; spectral evidence for sulfides, particularly in association with the hollows; and spectral evidence for the presence of water at the poles, such as hydroxylated minerals near polar impact craters with permanently shadowed floors.

2. Visible and Infrared Spectrograph

MASCS (McClintock and Lankton, 2007) consists of a Cassegrain telescope that simultaneously feeds VIRS and an Ultraviolet and Visible Spectrometer (UVVS). VIRS is a point spectrometer with a 0.023° field of view and two linear array detectors covering the wavelength range 300–1450 nm at 5-nm spectral resolution. A visible (VIS) detector is sensitive to wavelengths that extend from 300 to 900 nm, and a near-infrared (NIR) detector to wavelengths that extend from 900 to 1450 nm. Instrument temperature is modulated by orbital and seasonal variations in thermal load from Mercury and varies from 10 °C to >50 °C. The NIR detector is more susceptible to increased background and noise from elevated temperature than is the VIS detector, so the signal-to-noise ratio (SNR) of the VIS detector is typically at least 3–5 times greater than that of the NIR detector, and the NIR SNR becomes progressively lower at higher instrument temperatures.

For this paper we used the calibrated MASCS data products available from the Planetary Data System (PDS), and here we provide a brief overview of the calibration process with which these products were created. VIRS measures the radiance of sunlight scattered from the surface of Mercury. This radiance, L, carries units of W m^{-2} sr^{-1} μm^{-1} and is proportional to the instrument output through the relation

$$L = \left(\frac{(C - B_e - B_d - B_g)}{t}\right)\left(\frac{1}{S}\right) \quad (1)$$

where C is the raw data number (DN) value, B_e is a background due to an electronic offset (in DN), B_d is the temperature-dependent dark current background (in DN), B_g is a background offset resulting from grating-scattered light (in DN), and t is the integration time (in s). The radiometric sensitivity, S, is defined as the ratio of the instrument output rate to a known input radiance as measured in the laboratory and specified in units of DN s^{-1} (W m^{-2} sr^{-1} μm^{-1})$^{-1}$. The instrument's radiometric sensitivity, also known as the absolute radiometric calibration, was validated by Holsclaw et al. (2010) from a comparison of observations of the star Sirius with Earth-based measurements; agreement was found to within 10% over most of the spectral range 320–700 nm. Because of MESSENGER's highly eccentric orbit and the associated varying heat load from the planet, detector temperature can vary substantially over the course of any single observation sequence. As the temperature-dependent background B_d constitutes a large fraction of the observed signal, especially in the NIR channel, it is critical that this term be estimated accurately. A combination of backgrounds B_e and B_d was measured by engaging a shutter, which blocks light to the instrument, every 5th, 20th, or 40th spectrum, depending on observation type. A polynomial fit was used to interpolate the background output of each pixel as a function of temperature for each observation sequence. A residual offset, B_g, interpreted as light scattered from the grating, is present following background subtraction. This offset, assumed to be uniform (i.e., constant with wavelength), was determined for each spectrum by measuring the signal at wavelengths below the short-wavelength cutoff of the VIS channel.

After calibration of the VIRS data to spectral radiance, we derived the radiance factor (often denoted I/F) by dividing by the predicted radiance from a Lambertian surface illuminated normally by the Sun at the same distance:

$$r = \frac{L}{E_{Sun}/\pi} \quad (2)$$

where E_{Sun} is the solar spectral irradiance (in W m^{-2} μm^{-1}). We used the observed solar spectrum of Thuillier et al. (2003), convolved to match the spectral resolution of VIRS.

To facilitate a direct comparison of absolute reflectance between any two measurements obtained at an arbitrary viewing geometry, we employed a photometric normalization. Following the approach of Hillier et al. (1999), we modeled the dependence of reflectance on viewing geometry, represented by the function f, as the combination of a Lommel-Seeliger term representing isotropic scattering and a phase function to represent directional effects:

$$f(i, e, \alpha) = \frac{\cos i}{\cos i + \cos e} p(\alpha) \quad (3)$$

where i, e, and α are the incidence, emission, and phase angles for a given observation, and $p(\alpha)$ is the phase function. A linear relation was found to represent the phase function adequately:

$$p(\alpha) = a_0 + a_1\alpha \quad (4)$$

where $a_0 = 0.0576$, $a_1 = -3.52 \times 10^{-4}$, and the phase angle α is in degrees. These parameters were found not to change markedly between 400 nm and 700 nm, implying that any variation in the slope of the line with wavelength (e.g., phase reddening) is small. Although phase reddening has been demonstrated previously for Mercury (Holsclaw et al., 2010) from observations by MDIS and MASCS prior to orbit insertion, we consider the lack of evidence

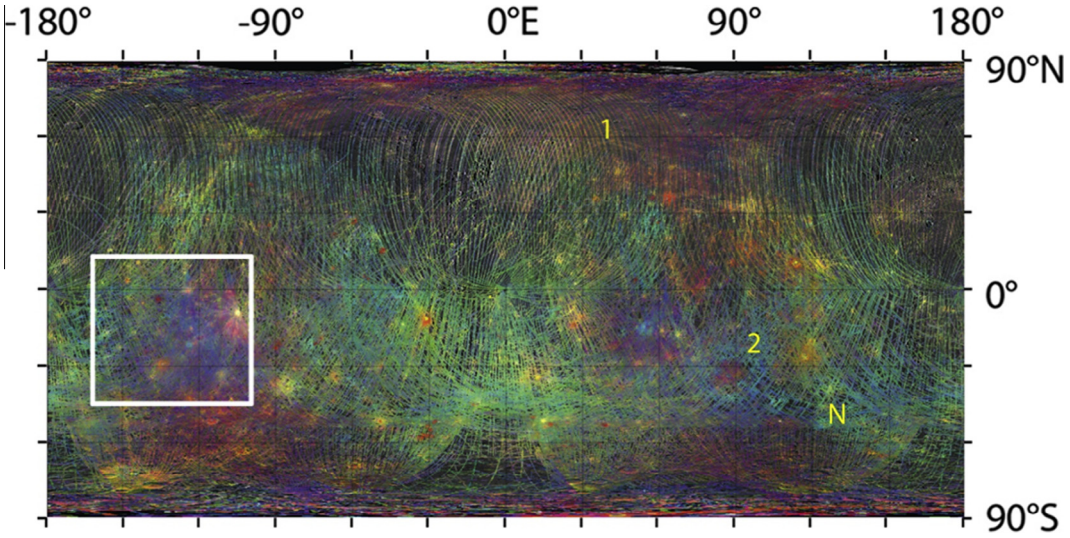


Fig. 1. Color composite in simple cylindrical projection centered on 0° latitude and longitude, for orbital observations from March 2011 to March 2012 superimposed over a monochrome MDIS global image mosaic at 750 nm. Red channel is R575, stretched between values of 0.03 and 0.10. Green channel is VISr, stretched between 0.50 and 0.65. Blue channel is UVr, stretched between 0.62 and 0.75. Grid spacing is 30° in latitude and longitude. Location "1" is a region of northern plains (Head et al., 2011), "2" marks plains around Rembrandt basin, and "N" marks Neruda crater. The white box outlines the area shown in Fig. 2.

in the MASCS orbital data to result from the restricted range of phase angles sampled.

Because of Mercury's proximity to the Sun, limitations on spacecraft pointing result in phase angles for MASCS that range from $\alpha = 78°$ to 102°. Most of the planet was observed at the minimum phase angle possible, between 78° and 80°, though the southernmost latitudes are observable only at α near 102°. The majority of libraries of laboratory spectral measurements of planetary analog materials contain spectra acquired with an incidence angle of 30°, an emission angle of 0°, and a phase angle of 30°, a standard adopted to confine spectral variations among samples to those resulting from mineralogy (e.g., Pieters, 1983). Normalization of MASCS observations to a typical laboratory geometry of $i = 30°$, $e = 0°$, $\alpha = 30°$ would involve extrapolation far beyond the range of angles of MASCS measurements and would likely result in large errors. We therefore chose to normalize all data to a viewing geometry of $i = 45°$, $e = 45°$, and $\alpha = 90°$. Thus, the normalized reflectance for a given observation is

$$r'(45, 45, 90) = r(i, e, \alpha)\frac{f(45, 45, 90)}{f(i, e, \alpha)} \quad (5)$$

3. Global spectral diversity

The MASCS coverage of Mercury during MESSENGER's primary orbital mission (18 March 2011 to 17 March 2012) is shown in Fig. 1. The size of the MASCS footprint varies systematically with integration time, altitude, and slant angle to the surface, ranging from 0.1 km (cross-track) × 3 km (down-track) to over 6 × 7 km. Systematic mapping of Mercury has allowed VIRS to sample all geologic regions. The false-color composite presented in Fig. 1 includes all MASCS observations of the illuminated surface with $i < 88°$ for latitudes between 83°N and 83°S. At higher latitudes, higher incidence angles were included. Colors have been chosen to highlight the overall visible albedo, using the reflectance at 575 nm wavelength (R575, red); the spectral slope at visible and infrared wavelengths, represented by the ratio of reflectance at 415 nm to that at 750 nm (VISr, green); and the spectral slope at ultraviolet (UV) and visible wavelengths, represented by the ratio of reflectance at 310 nm to that at 390 nm (UVr, blue).

Some of the relations between spectral variations and geologic features are illustrated in an expanded view of the Tolstoj–Beethoven area of Mercury in Fig. 2. This ~5×10^6 km^2 region includes medium-reflectance, high-UVr plains; LRM material (Robinson et al., 2008) concentrated in a ring around the Tolstoj basin; pyroclastic materials (Kerber et al., 2009, 2011; Goudge et al., 2012); and fresh crater floors and ejecta. Fresher materials exposed by young impact craters have higher reflectance at all wavelengths and the highest VISr value of all units on Mercury. Individual color terrains correspond approximately to those mapped from MDIS multispectral images (Robinson et al., 2008; Denevi et al., 2009). Ejecta from small craters and other relatively fresh materials show an outward gradation in spectral properties, notably in overall brightness and VISr value, consistent with lateral mixing of ejecta with surrounding materials at increasing radial ranges. In addition, some morphologically fresh craters have reduced contrasts relative

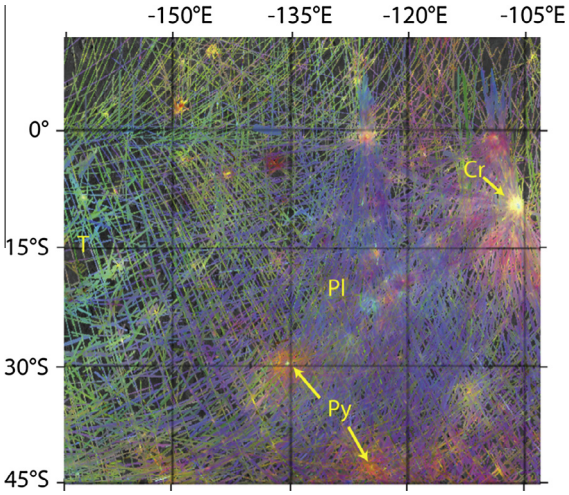


Fig. 2. Expanded view of the Tolstoj–Beethoven area (13°N to 45°S, −161°E to −102°E) within the white box in Fig. 1. Low-reflectance blue plains (Pl) appear in purple, and LRM around the Tolstoj basin (T, centered at 16.2°S, −164.7°E) appears cyan. Pyroclastic deposits (Py) in and around craters appear orange and red. Fresh crater materials (Cr) are bright yellow.

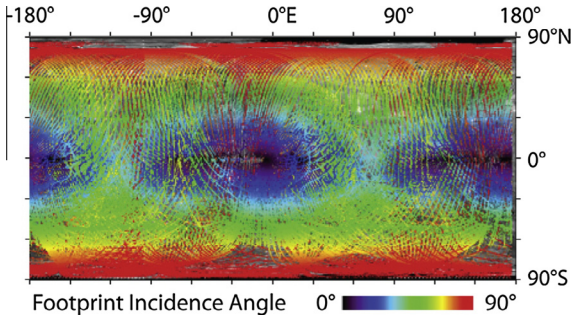


Fig. 3. Map of incidence angle for the observations in Fig. 1. Background mosaic and map projection are as in Fig. 1.

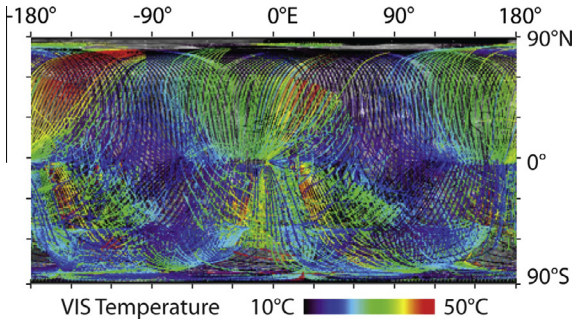


Fig. 4. Map of instrument temperature (°C) for the observations in Fig. 1. Background mosaic and map projection are as in Fig. 1.

to surrounding materials, consistent with darkening and reddening due to space-weathering processes (McClintock et al., 2008; Riner and Lucey, 2012).

Viewing geometry and instrument conditions varied during the global observations of spectral reflectance, as illustrated in Figs. 3 and 4. In general, there is no evident correlation between the map of VIRS-derived spectral reflectance and maps of viewing angles or instrument temperature. Such a lack of correspondence indicates that the instrument calibration and photometric normalization have successfully removed these effects from the VIRS data. Notable exceptions include polar latitudes, which could be observed only at very high incidence angles, producing high-latitude shadowing effects in the observations (Fig. 1).

4. VIRS spectral units

For this paper we employed a supervised method that exploited spectral parameters to divide the surface of Mercury into four broad VIRS spectral units, here termed "average," "dark blue," "red," and "bright." We examined spectra of locations across Mercury that represent a wide range of morphologic and color variations, and we defined spectral units on the basis of differences from the planetary mean values of the three spectral parameters R575, VISr, and UVr. Because Mercury's spectrum is dominated by a steeply red continuum with no strong mineral absorptions, expressing spectra as ratios to a planetary mean accentuates spectral differences from an average for the planetary surface. The planetary mean spectrum, shown in Fig. 5a, was derived from more than 850,000 spectra acquired globally (with $i < 65°$, $e < 80°$, and detector temperatures < 30 °C).

A complementary study of the MASCS dataset with an unsupervised classification approach was performed by Helbert et al. (2013a). Those workers applied a hierarchical clustering analysis technique (Michaud, 1997; Everitt et al., 2011) to six spectral bands that span the wavelength range from 540 to 700 nm. The unsupervised classification approach indicates two global surface units, termed the polar and equatorial regions. In general the unsupervised classification method allows an objective assessment of spectral variations on a global scale, whereas the supervised classification approach adopted in this paper highlights variations on the scale of individual features and smaller geological units.

Spectra from 100 locations were chosen on the basis of geomorphic, MDIS color, and spectral parameter variation to represent the diversity of spectral types on Mercury's surface. The four spectral types and the variations across spectral type are illustrated with a subset of 15 spectra in Fig. 5b. Ratios of those spectra to the average spectrum for Mercury are displayed in Fig. 5c. The locations of the regions for which spectra are shown in Fig. 5 are given in Table 1.

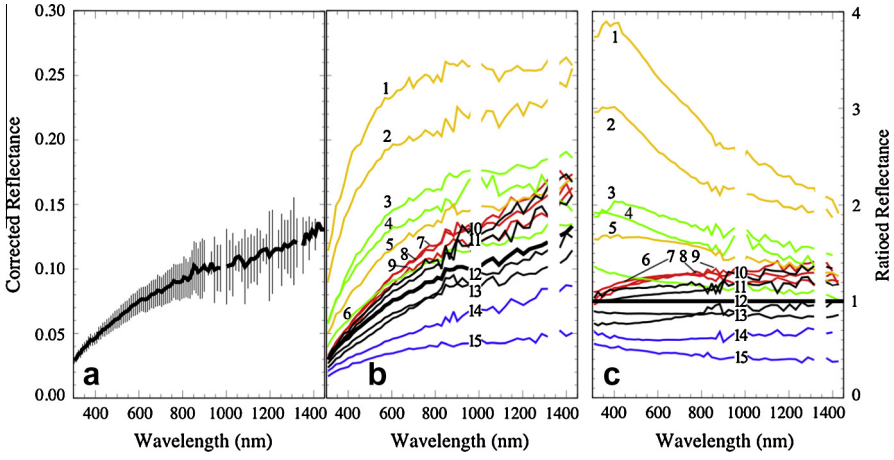


Fig. 5. (a) Average reflectance spectrum for Mercury. Error bars indicate ±2 standard deviations of the data in each wavelength bin (each bin is an average of four ~2.3-nm-wide spectral pixels for the visible detector and six pixels for the near-infrared detector). Noise levels at detector temperatures of 30 °C are approximately 0.2% of the signal in the visible detector and ~5% of signal in the near-infrared detector. Breaks near 980 nm and 1350 nm denote the NIR pixels that first saturate as a result of increased background signal at elevated instrument temperatures. These pixels were removed for uniform comparison. (b) Representative spectra for VIRS spectral unit types, from ultraviolet to near-infrared wavelengths and binned into 18.6-nm-wide bands in the spectral range 300–900 nm and 30-nm-wide bands for the spectral range 900–1450 nm. Numbers correspond to the regions identified in Table 1. Examples of the average VIRS spectral unit are shown in black (numbers 10–13); those of the dark blue unit are shown in blue (numbers 14, 15); those of the red unit are shown in red (numbers 7–9); and those of the bright unit are shown in orange (bright fresh craters, numbers 1, 2, 5) and green (hollows, numbers 3, 4, 6). The planetary mean spectrum from (a) is plotted as a thick black line. (c) Same spectra as in (b) ratioed to the planetary mean spectrum.

Table 1
Locations of the spectra in Fig. 5.

Spectrum	Latitude, °N	Longitude, °E	Description	VIRS spectral unit
1	15.77	−155.25	Small fresh crater	Bright
2	3.77	−169.19	Small fresh crater	Bright
3	4.31	−148.50	Tyagaraja hollows	Bright
4	42.48	154.32	Sander hollows	Bright
5	15.74	−156.30	Less fresh crater	Bright
6	28.27	−60.24	Praxiteles hollows	Bright
7	−20.80	−74.48	Raphael pyroclastic deposit	Red
8	14.73	−49.19	Lermontov pyroclastic deposit	Red
9	5.38	−55.96	Mistral pyroclastic deposit	Red
10	66.63	18.812	Northern plains	Average
11	36.16	151.75	Caloris plains	Average
12	−29.95	−8.61	0°E plains	Average
13	−57.81	106.86	Southern plains east	Average
14	29.41	59.87	Rachmaninoff floor	Dark blue
15	−2.88	−41.73	Titian ejecta	Dark blue

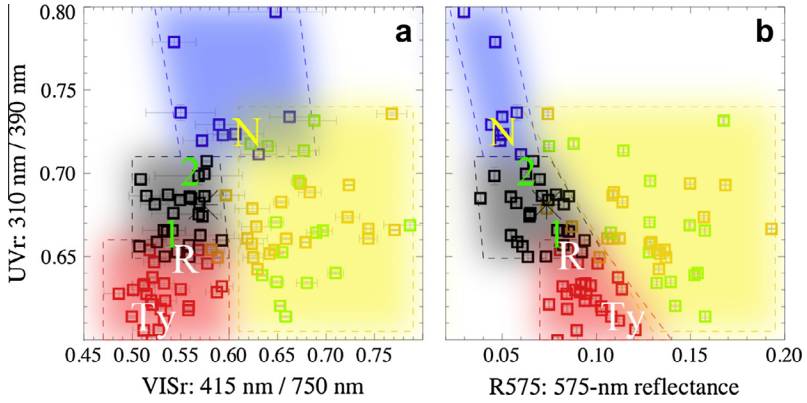


Fig. 6. VIRS spectral parameters compared for 100 locations on Mercury's surface, including the example areas for which spectra are shown in Fig. 5. (a) UVr versus VISr. (b) UVr versus R575. Squares marking individual locations are color-coded by VIRS spectral unit type: black = average unit; blue = dark blue unit; red = red unit; green or orange = bright unit (green for hollows materials, orange for crater floors and ejecta of varying freshness). Shaded regions show the global range of each VIRS spectral unit. The planetary mean spectrum is represented by the black asterisk. Spectra for northern plains (1) and plains around Rembrandt basin (2) show the range of variation within the average VIRS spectral unit. Spectra for pyroclastic materials in Raphael (R) and Tyagaraja (Ty) show the range of variation within the red VIRS spectral unit. The region around crater Neruda (for which the combination of spectral parameters is marked with an N) corresponds to the area of highest Fe/Si ratio measured with the MESSENGER XRS (Weider et al., 2013).

Variations in spectral parameters for all 100 locations are plotted in Fig. 6. UVr is plotted versus VISr in Fig. 6a and versus R575 in Fig. 6b. In these displays, spectra of similar geological or morphological types depart in consistent directions from the planetary mean, permitting us to define VIRS spectral units on the basis of these groupings.

4.1. Average VIRS spectral unit

The average VIRS spectral unit includes spectra for which R575 reflectance is within 25% of the mean planetary reflectance across the VIRS spectral range, has a UVr value between 0.64 and 0.71, and has a VISr value between 0.5 and 0.6 (shown in black in Figs. 5 and 6). The majority of Mercury's surface falls in this category, which includes plains units that can also be distinguished by morphology or visible-wavelength color (Robinson and Lucey, 1997; Denevi et al., 2009). The variation of spectra within the average unit accounts for much of the observed color variation in the global spectral map (Fig. 1). For example, the labels "1" and "2" in Figs. 1 and 6 denote two example plains locations that cover the range of spectra within the average VIRS spectral unit. Location 1 in Fig. 1 is in the northern plains (Head et al., 2011) and falls in the brighter, redder portion of the average unit's spectral parameter space. Location 2 in Fig. 1 is darker and bluer and is in the plains surrounding Rembrandt basin. Most spectra with parameters outside the average VIRS spectral unit boundaries are geologically and morphologically as well as spectrally distinct from plains units.

4.2. Dark blue VIRS spectral unit

The dark blue VIRS spectral unit (shown in blue in Figs. 5 and 6) is characterized by spectra that are both darker than the planetary mean spectrum and less red-sloped or "bluer" (with UVr > 0.71 and VISr > 0.55). The dark blue unit includes all areas identified as LRM from MDIS images (Robinson et al., 2008; Denevi et al., 2009) and grades into low-reflectance blue plains. The unit boundaries are defined primarily by the spectral limits of LRM materials. Virtually no locations on Mercury that are not LRM or low-reflectance blue plains fall in this spectral unit. Locations of the dark blue VIRS spectral unit include the area surrounding the Tolstoj basin ("T" In Fig. 2) and a region in Praxiteles crater near a small hollows unit (Fig. 7c, blue arrow).

4.3. Red VIRS spectral unit

The red VIRS spectral unit is characterized by spectra (shown in red in Figs. 5 and 6) that are both higher in reflectance and "redder" than the planetary mean spectrum, with low UVr and VISr (<0.66 and <0.60, respectively). The red unit includes pyroclastic deposits defined on the basis of morphology and visible color as

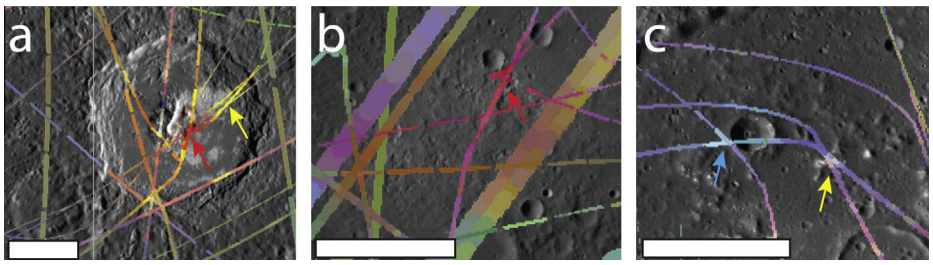


Fig. 7. Sample locations of and spatial relations among VIRS spectral units. VIRS footprints are shown in the same color coding as in Figs. 1 and 2. Scale bars each denote 40 km. (a) Hollows in the bright VIRS spectral unit (yellow arrow) lie near pyroclastic materials of the red VIRS spectral unit (red arrow) within Tyagaraja crater (96.9 km diameter, centered at 3.9°N, −148.7°E). (b) Pyroclastic material with higher UVr and VISr values and lower reflectance within the red VIRS spectral unit (red arrow) on the floor of Raphael crater (350 km diameter, centered at 20.87°S, −74.46°E). (c) Hollows material in the bright VIRS spectral unit (yellow arrow) within Praxiteles crater (182 km diameter, centered at 28.20°N, −60.28°E) is near material of the dark blue VIRS spectral unit (blue arrow).

having formed through explosive volcanism (e.g., Head et al., 2008; Kerber et al., 2009, 2011; Goudge et al., 2012). Also included in this spectral unit are parts of the smooth plains at high northern and southern latitudes, as well as the smooth plains interior to the Caloris basin. The unit boundaries are defined primarily by the spectral limits of pyroclastic materials and high-reflectance red plains units such as the northern plains.

Example pyroclastic materials within the red VIRS spectral unit exhibit a range of spectral parameters (Fig. 7). Inside crater Tyagaraja (Fig. 7a, red arrow), for instance, the pyroclastic materials have relatively high reflectance and steeper visible through near-infrared spectral slope. This area is shown in Fig. 6 (label "Ty") to be in the low-UVr, low-VISr, high-R575 region of the parameter space for the red unit. A pyroclastic region inside Raphael impact crater (Fig. 7b, red arrow), in contrast, is among the least bright of the pyroclastic materials, with a spectral slope near the planetary average. This area is shown in Fig. 6 (label "R") to be in the high-UVr, high-VISr, low-R575 region of the parameter space for the red VIRS spectral unit, close to the lowest UVr values and brightest materials of the average VIRS spectral unit.

4.4. Bright VIRS spectral unit

The bright VIRS spectral unit is characterized by spectra (shown in yellow and green in Figs. 5 and 6) that cover a wide range of UVr (0.60–0.74) and are generally brighter and have a higher VISr value than the highest-reflectance areas of the average unit. Hollows (Blewett et al., 2011, 2013), shown in green in Figs. 5 and 6, have spectral parameters that fall within the bright VIRS spectral unit and can be further subdivided into high-UVr, intermediate-UVr, and low-UVr hollows (Fig. 8). High-UVr hollows (UVr > 0.69) tend to be located near areas of the dark blue VIRS spectral unit. For example, the high-UVr hollows region inside Praxiteles crater ("P" in Fig. 8, yellow arrow in Fig. 7c) borders an area of the dark blue VIRS spectral unit. Low-UVr hollows (UVr < 0.64) tend to be located near areas of the red VIRS spectral unit. For example, hollows inside Tyagaraja crater ("Tyh" in Fig. 8, yellow arrow in Fig. 7a) are adjacent to pyroclastics of the red VIRS spectral unit.

Areas of the bright unit also include those materials with the highest surface reflectance on Mercury. These areas of high reflectance and high VISr values coincide almost exclusively with the brightest, most morphologically fresh impact craters. These craters have a nearly flat spectrum in the near-infrared (VISr > 0.72) and moderate slopes in the UV (UVr between 0.64 and 0.70). Bright craters and ejecta trend toward the average VIRS spectral unit with decreasing apparent freshness, probably indicating a crater age–maturity trend (e.g., Matson et al., 1977; Blewett et al., 2009). Fig. 9 shows sample locations of the bright VIRS spectral unit in the ejecta of two small, fresh-looking craters. Crater "1" in Figs. 8 and 9 is one of the brightest, morphologically freshest craters observed by VIRS (and corresponds to location 1 in Table 1), whereas for crater "5" in Figs. 8 and 9 and Table 1, although the feature is still within the bright VIRS spectral unit, the ejecta has a more subdued morphology and may be less pristine.

Hollows with intermediate UVr values and less pristine impact craters both lie in the central parameter space of the bright VIRS spectral unit. These two categories of features cannot be readily distinguished on the basis of spectral reflectance, but they are easily identified from images.

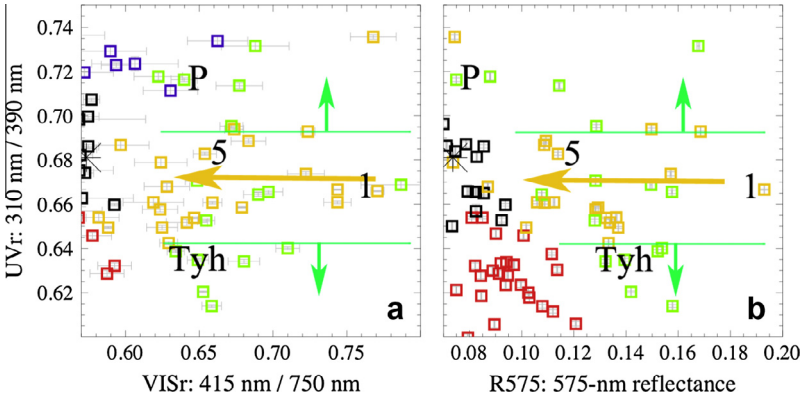


Fig. 8. Expanded view of the variation of VIRS spectral parameters for the bright VIRS spectral unit region of Fig. 6. High-UVr hollows all lie above the line at UVr = 0.69. High-UVr hollows in Praxiteles (P) are near the dark blue VIRS spectral unit in parameter space. Low-UVr hollows all lie below UVr = 0.64. Low-UVr hollows in Tyagaraja (Tyh) lie near the red VIRS spectral unit parameter space. The yellow arrow denotes the trend of apparent evolution of color for impact craters from fresh, pristine, high-R575, and high-VISr (1) material toward more spectrally average material (5).

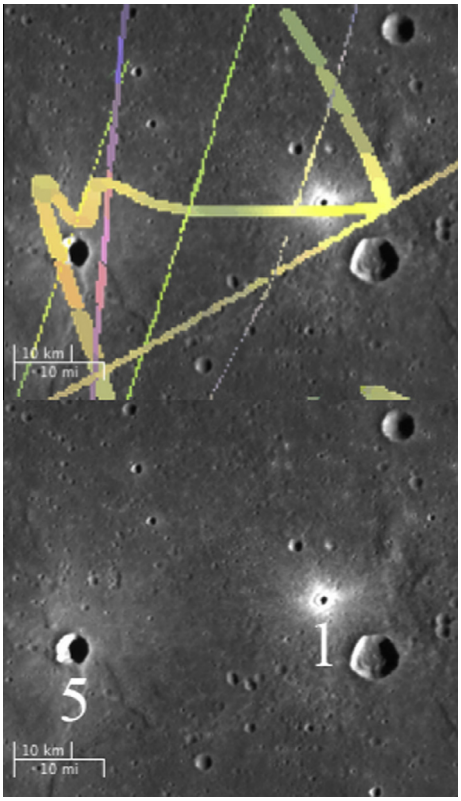


Fig. 9. Two examples of impact craters that fall in the bright VIRS spectral unit. VIRS footprints are shown in the upper version of the MDIS image mosaic with the same color coding as in Figs. 1 and 2. Crater "1" is among the brightest and freshest appearing on Mercury and is labeled "1" in Fig. 8 and Table 1. Crater "5," so labeled in Fig. 8 and Table 1, is somewhat less fresh looking relative to the surrounding plains. The portion of the global MDIS mosaic shown is centered at 15.82°N, −155.70°E.

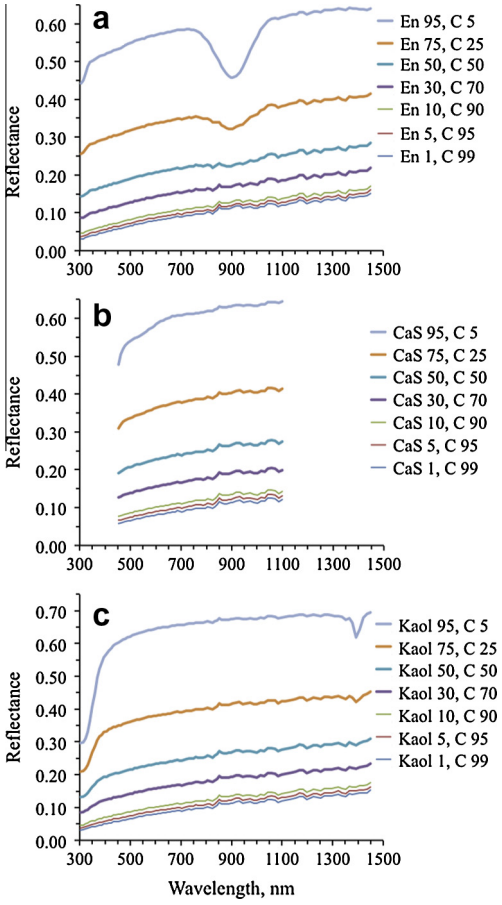


Fig. 10. Predicted spectra from mixing models of measured spectra of laboratory samples and VIRS spectra of Caloris plains material. (a) Spectra for seven different mixtures of RELAB low-iron pyroxene ($En_{97.5}$) with Caloris interior plains material (C). Fractions shown are weight percentages. (b) Spectra for seven different mixtures of heated oldhamite (CaS) (Helbert et al., 2013b) with Caloris plains material. (c) Spectra for seven different mixtures of RELAB crystalline kaolinite (Kaol) with Caloris plains material.

5. VIS–NIR spectral variation

5.1. Fe^{2+} abundance

One of the most striking aspects of reflectance spectra of Mercury is the lack of strong absorption features, particularly near 1 μm, a wavelength near which octahedrally coordinated ferrous iron contributes an absorption in silicate minerals (Burns, 1993). Maps of band depth derived with several methods for determining absorption features near 1 μm have resolved no features unequivocally distinguishable from the noise anywhere on Mercury. Even in the freshest (least space-weathered) exposures of the bright VIRS spectral unit, no clear 1 μm band is present. In laboratory measurements of pure phases, even a trace amount of FeO (<0.5 wt%) structurally bound in the M2 site of pyroxenes produces a measurable absorption band (Klima et al., 2011). Absorption bands are diminished by the presence of strong absorbers such as nanophase iron produced by space weathering (e.g., Pieters et al., 2000; Hapke, 2001; Noble and Pieters, 2003), or opaque minerals, plausibly including metallic iron, troilite, ilmenite, or graphite. Thermospectral effects due to heating (Hinrichs and Lucey, 2002; Helbert and Maturilli, 2009; Izenberg et al., 2012; Helbert et al., 2013b), vitrification as a result of thermal cycling (Helbert and Maturilli, 2009; Helbert et al., 2013b), or agglutination from impact melting (e.g., Cintala, 1992) may further reduce spectral absorption features.

We conducted spectral modeling to assess the detectability of FeO in silicates by VIRS. We modeled binary mixtures of a low-iron orthopyroxene ($En_{97.5}$, RELAB spectrum DL-CMP-064) with the average VIRS reflectance spectrum of the volcanic plains interior to the Caloris basin (spectrum 11 in Fig. 5 and Table 1), chosen as representative of extensive areas of bright plains materials on Mercury. The VIRS spectrum for Caloris plains material contains no identifiable absorptions, other than a drop in reflectance toward the UV, likely caused by oxygen–metal charge transfer (OMCT) absorptions (McClintock et al., 2008). Caloris plains material is thus spectrally similar to the artificial, spectrally neutral end-member used by Lucey and Riner (2011) in their modeling of Mercury's reflectance. We employ the spectrum for Caloris plains material in our mixing analysis because it inherently includes the effects of space weathering and darkening agents as well as the noise typical of VIRS observations. For our modeling, the Caloris and laboratory spectra were converted to single-scattering albedo (SSA) following the procedures of Mustard and Pieters (1989). The equations of Hapke (2012) were employed to combine SSAs using weight fractions, area-weighted by particle sizes and mineral densities, and then to calculate the bidirectional reflectance of the mixture at an incidence angle of 45°, an emission angle of 45°, and a phase angle of 90°. Densities of the $En_{97.5}$ sample and Caloris plains material were both assumed to be 3.2 g/cm^3. The particle size for the components was set to 15 μm. The resulting mixed spectra are shown in Fig. 10a. In the figure, a mixture of 95% $En_{97.5}$ by weight with Caloris plains material shows a clear, easily discernable 1-μm absorption band, even with an increase in VIRS

Table 2
Band depth calculations for mixing models.

Mineral	Continuum 1 (nm)	Continuum 2 (nm)	Band center (nm)	Avg. noise at band center
Enstatite ($En_{97.5}$)	731	1043	889	0.012
Oldhamite CaS	490	611	555	0.0016
Kaolinite	1365	1421	1393	0.028

detector noise with wavelength in the infrared (Fig. 5a). A mixture with 75% $En_{97.5}$ has a substantially reduced absorption band at 1 μm, but such a band is probably still distinguishable by VIRS. A mixture with 50% $En_{97.5}$ exhibits only a weak absorption feature.

To quantify detectability, we compared simple three-point band depths with fractional noise of the VIRS spectrum at the albedo of Caloris interior plains material. Band depths for each absorption were calculated by projecting a straight line between two continuum points and calculating the reflectance on that line at the central wavelength of the band. The fractional band depth was then measured as $1-(R_b/R_c)$, where R_b is the reflectance at the band center and R_c is the continuum reflectance at the wavelength of the band center. Continuum and band center wavelengths are given in Table 2, along with the typical percentage of noise at the wavelength of the absorption. Because each of the points is subject to noise, we consider that band depths less than ~5 times the typical noise value are not resolvable.

For the mixture with 95% $En_{97.5}$, the derived 1-μm band depth was 19.0 times greater than the VIRS fractional noise at the albedo of Caloris interior plains. The band depth of the mixtures with 75% and 50% $En_{97.5}$ were 10.4 and 5.7 times greater than the noise, respectively. The mixture with 50% $En_{97.5}$ is thus at the threshold of detectability for VIRS. An orthopyroxene with 97.5% enstatite by mole contains 1.83 wt% FeO, or 1.43 wt% Fe^{2+}. Thus, if Caloris plains material has no Fe in its silicates, the detectability envelope of Fe^{2+} in silicates for VIRS begins at ~0.7 wt% Fe^{2+} (~0.9 wt% FeO). If, in contrast, the silicates in Caloris plains material contain the maximum Fe^{2+} that would be detectable if the band signature is similar to that in $En_{97.5}$, then the detectability threshold would double to ~1.4 wt% Fe^{2+} (~1.8 wt% FeO). The similarity of the spectrum for Caloris plains material and that for Lucey and Riner's (2011) iron-free silicate model may support an argument that the higher threshold is less likely, but we may conclude with some conservatism that iron in silicates in the surface materials of Mercury cannot exceed ~1.4 wt% Fe^{2+} (~1.8 wt% FeO).

The generally low Fe^{2+} content of surface silicates indicated by the MASCS observations is consistent with the inference from XRS measurements that the total iron abundance at Mercury's surface is typically between 0.75 and 2.5 wt% (Weider et al., 2013; Izenberg et al., 2013). The MASCS results also agree with earlier ground-based spectral observations interpreted to indicate an Fe^{2+} content of surface silicates of less than 3 wt% (Vilas, 1985; Warell, 2003).

5.2. Minor phases – sulfides

In light of the discovery of Mercury's high (1–4 wt%) sulfur content by the XRS and GRS instruments (Nittler et al., 2011; Evans et al., 2012), the correlation of Ca and S abundances on Mercury's surface (Nittler et al., 2011; Weider et al., 2012), and the curious morphology of hollows, Blewett et al. (2013) and Helbert et al. (2013b) suggested that hollows (and/or LRM) may be associated with higher than average abundances of sulfide minerals such as CaS. Spectra of meteoritic CaS and synthetic CaS and MgS measured in the laboratory (Burbine et al., 2002; Helbert et al., 2013b) exhibit a subtle absorption band near 500–600 nm. We attempted to detect this band with continuum-removal band depth estimation methods at a number of different wavelengths in this spectral region (e.g., continuum anchors in the range 400–500 nm on the short-wavelength end and 650–750 on the long-wavelength end, and band centers from 450 to 650 nm), as well as curve fitting and differencing methods, and we found no clear evidence for this absorption in the vicinity of hollows or any other surface unit.

Heating sulfides to Mercury daytime temperatures tends to suppress this diagnostic feature. For MgS, the band strength after a single exposure to Mercury's daytime temperature is reduced by 90%. The band strength reduction for CaS is more moderate, and heating followed by cooling yields a comparable absorption band depth (Helbert et al., 2013b). We used a spectrum for once-heated oldhamite (CaS) from Helbert et al. (2013b) in our spectral mixing model with Caloris plains material to assess the detectability of sulfides by VIRS (Fig. 10b). An analysis of three-point band depths (see Table 2 for center wavelengths) results in a ratio of band depth to noise of 8.4 for a mixture with 95% CaS by weight and 4.9 for a mixture with 75% CaS. If Caloris plains material contains no sulfur, an area would have to contain more than 75% CaS for an absorption band to be detected by VIRS. If Caloris plains material has a sulfur content of 1–4 wt% S (e.g., 2–9 wt% CaS), then the detection threshold would be even greater, ~77–84% CaS by weight. The brightening effects of a pure sulfide might be detectable at lower concentrations, but they would not be easily distinguishable from other brightening processes in the absence of absorption features. VIRS observations thus may rule out the presence of areally extensive (on the scale of a few square kilometers) pure sulfide phases on the surface of Mercury, but substantial concentrations, even over large areas, could escape detection.

5.3. Minor phases – hydroxyl

Mercury's polar deposits imaged by Earth-based radar (e.g., Slade et al., 1992; Harmon et al., 2011) are confined to regions in permanent shadow, predominantly within high-latitude impact craters (e.g., Chabot et al., 2012). On the basis of neutron spectrometry (Lawrence et al., 2013), active measurement of near-infrared reflectance (Neumann et al., 2013), and thermal modeling with measured topography (Paige et al., 2013), water ice must be a major constituent of polar deposit material. Alteration minerals formed in the presence of water have been observed on asteroids (e.g., Vilas et al., 1994; Vilas and Sykes, 1996) and possibly the Moon (Vilas et al., 1999, 2008; Pieters et al., 2009).

Although VIRS cannot view the permanently shadowed regions of Mercury, it is possible that alteration minerals might be present near the permanently shadowed regions as a result of impact-induced reaction of rock with water ice. Typical alteration minerals, such as clays, exhibit diagnostic absorption bands near ~1.4 μm, within the nominal wavelength range of VIRS, associated with metal–OH bonds. Thermal noise in the infrared detector, however, precludes identification of weak, narrow features near 1.4 μm. Moreover, experiments simulating hypervelocity impacts into phyllosilicate regoliths have shown that interlayer water is removed during the impact process (Thibault et al., 1997; C.A. Thibault, personal communication, 2013).

A broad absorption feature near 0.7 μm has been observed on a large number of low-albedo bodies thought to contain hydrated minerals (Vilas et al., 1994, 2006). This feature results from an intervalence charge transfer between Fe^{2+} and Fe^{3+}. Such an absorption has not been observed on Mercury, however, and it is unlikely to be present given the low iron abundance in surface silicates as well as Mercury's chemically reducing environment.

We applied our mixing model analysis to an iron-free hydrated silicate (crystalline kaolinite, RELAB spectrum CY-PLH-017/C1CY17), with results shown in Fig. 10c. An analysis of three-point band depths (see Table 2 for center wavelengths) yields a ratio of band depth to noise of 3.1 even for a mixture with 95% kaolinite by weight, because of the elevated noise levels of VIRS near the wavelength of this absorption. Thus, even nearly pure hydrous phases may not be detectable by VIRS.

6. UV spectral variations

Although no definitive crystal-field absorption band has been detected in surface reflectance spectra of Mercury at visible and NIR wavelengths, possible observations of an OMCT band at UV to visible wavelengths have been reported (McClintock et al., 2008). Evidence for such a band is exhibited in several ratioed spectra in Fig. 5c, particularly in the bright VIRS spectral unit spectra from the freshest craters and brightest hollows (spectra 1–5 in Fig. 5), which show UV downturns shortward of 400 nm relative to the average planetary spectrum.

OMCT absorptions occur between oxygen and transition metals such as Fe and Ti (e.g., Cloutis et al., 2008) and are one to two orders of magnitude stronger than crystal field absorptions (e.g., Burns, 1993). They are sensitive to even trace amounts (<0.01 wt%) of Fe^{3+} and Fe^{2+} (Cloutis et al., 2008). The major Fe^{3+}–O charge-transfer absorptions occur at shorter wavelengths (~210–230 nm) than the Fe^{2+}–O absorptions (~250–270 nm) and are more intense (Cloutis et al., 2008). Given the lower abundance of Ti (<1%) than of Fe (1–4 wt%) on Mercury indicated by MESSENGER XRS and GRS measurements (Nittler et al., 2011; Evans et al., 2012), Fe is a more plausible source than Ti for an OMCT band on Mercury.

Many of the materials with OMCT absorptions documented in the laboratory exhibit a shoulder in the reflectance near 400 nm and a sharp slope toward decreasing wavelengths, features detectable with VIRS observations. Measurements of the ultraviolet reflectance spectra of several minerals at wavelengths between 200 and 400 nm (Cloutis et al., 2008) show that some exhibit an absorption edge between 300 and 400 nm, but some do not. VIRS observations rule out the presence of substantial magnetite, which has a weak absorption feature centered at 350 nm (Cloutis et al., 2008), but such a mineral is unlikely given the low oxygen fugacity of Mercury surface material (Riner et al., 2010; McCubbin et al., 2012). The TiO_2 polymorphs anatase and rutile have absorption minima near 350 and 390 nm, respectively, features that are not visible in VIRS data and would be unlikely given the low average titanium abundance measured by XRS as noted above. Although MESSENGER observations cannot confirm or rule out the presence of other metals that give rise to OMCT bands, such as vanadium or cobalt, the presence of a small amount of iron is sufficient to account for the observed spectra. The spectra of olivine, plagioclase, pyroxene, and basalt, for instance, show an absorption edge in the UV that could be seen with VIRS if present on Mercury (Cloutis et al., 2008).

Laboratory measurements of the reflectance spectra of low-Fe silicates (Klima et al., 2007, 2011) and glasses (Greenspon et al., 2012) have shown that as iron content decreases, reflectance at wavelengths above 300 nm increases, especially at visible wavelengths, and the OMCT absorption bands steepen and their centers move to shorter UV wavelengths (e.g., Fig. 11). An increase in total Fe content also drives the visible-wavelength shoulder to longer wavelengths for both glasses and silicates. The appearance of an OMCT-like absorption edge in Mercury spectra from VIRS and the variable UVr slope may thus be the result of spatial variations in the small amount of iron in surface materials. Support for a dependence of UVr on Fe content can be drawn from a comparison of XRS-derived Fe content with the VIRS UVr parameter (Izenberg et al., 2013). The highest Fe contents measured by XRS (Weider et al., 2013) correspond to the area near crater Neruda (marked "N" in Fig. 1), for which the spectrum has a relatively high UVr value (Fig. 6) and is similar to spectra 12–15 in Fig. 5.

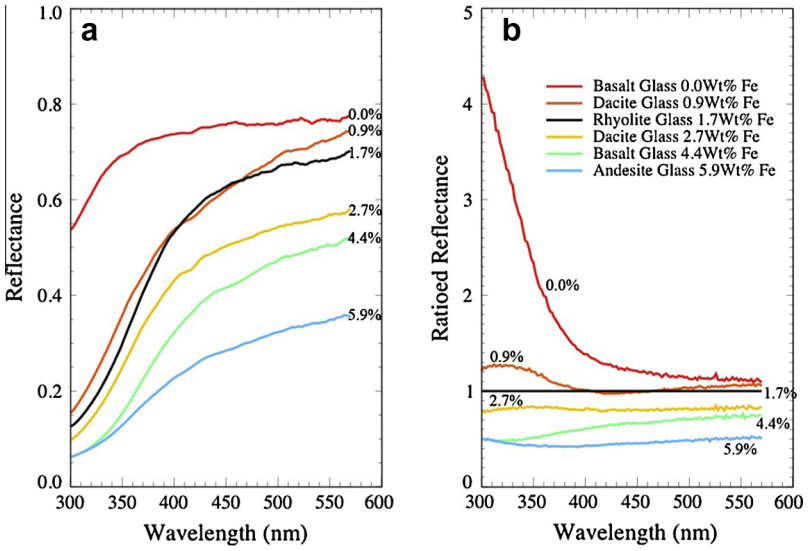


Fig. 11. Variation in spectral reflectance with Fe content (determined by electron microprobe analysis) in laboratory-synthesized glass powders (Greenspon et al., 2012). Glass types are classified by total alkali versus silica (Le Maitre et al., 2005), shown by wt% Fe. Higher Fe contents correspond to decreased reflectance at ultraviolet through visible wavelengths. (a) Reflectance of fine-grained (<10 μm) pure-glass powders at $i = -5°$, $e = 55°$, $\alpha = 60°$. (b) Reflectance spectra ratioed to that of the rhyolite glass sample with 1.7 wt% total Fe as a proxy for the average spectrum of Mercury.

In addition to the effects of iron in silicates, small amounts of metallic Fe can affect reflectance and spectral slope. Nanophase Fe (Noble et al., 2007) darkens and reddens surface material, whereas larger submicroscopic Fe particles that are not effective at reddening (Lucey and Noble, 2008; Lucey and Riner, 2011) mainly darken. The high UVr values, modest VISr slopes, and low reflectance of the dark blue VIRS spectral unit materials (e.g., LRM) could thus indicate somewhat higher Fe contents than other units, possibly as submicroscopic Fe. The low VISr and UVr and higher albedo of red VIRS spectral unit materials (e.g., pyroclastic deposits) conversely suggest lower Fe contents. The diversity of bright VIRS spectral unit materials (e.g., different types of hollows) could imply different compositions or mineralogies across morphologically similar terrains.

Another mineral that would show a steep positive slope in reflectance from 300 to 400 nm relative to the average spectrum of Mercury is solid SO_2 (Nash et al., 1980). The spectrum of SO_2 frost mixed with yellow sulfur also exhibits this spectral characteristic (Nash et al., 1980). The SO_2 frost is not stable within Mercury's daytime temperature environment, however (Vasavada et al., 1999). Spectra of other sulfur-containing minerals, such as MgS, show an absorption edge beginning closer to 500 nm and a decrease in reflectance with decreasing wavelength, features that do not match what is seen in MESSENGER VIS–NIR measurements (Helbert et al., 2013b).

7. Conclusions

Reflectance spectra of Mercury's surface obtained with MESSENGER's Mercury Atmospheric and Surface Composition Spectrometer allow four broadly distributed spectral units to be defined on the basis of spectral parameters. These units grade into one another, with no sharp break points. From the characteristics of these units and their relationships to geological terrains identified from multi-spectral imaging, several important conclusions may be drawn about the mineralogy of Mercury's surface.

1. Silicate minerals on Mercury's surface are Fe-poor. No crystal-field absorption band has been identified near 1 μm, even in the freshest exposures, though OMCT absorption features may imply the presence of some Fe. Modeling results confirm earlier inferences and suggest that mafic silicates on Mercury have no more than ~1.4 wt% Fe^{2+} (~1.8 wt% FeO). Some higher-UVr regions observed by VIRS correspond to areas with XRS-derived upper limits on iron abundance near 2 wt% Fe. The silicate mineralogy of Mercury is thus likely to be dominated by very low-Fe phases that are bright when freshly excavated (e.g., enstatite, feldspar). The surface is substantially darker than a laboratory mixture of any of those minerals, however, suggesting darkening by a combination of opaque phases (sulfides, metals such as submicroscopic iron, or oxides) and some combination of intense space weathering (Hapke, 2012; Riner and Lucey, 2012) and thermal cycling (Helbert and Maturilli, 2009).
2. There are systematic spectral variations that coincide with morphological boundaries on Mercury and suggest compositionally distinct materials. Terrain types that are distinct in both geology and spectral reflectance may differ in elemental or mineralogical composition.
3. Sulfide absorption bands have not been identified in VIRS data, even in locations, such as hollows (Blewett et al., 2011, 2013), where sulfides are hypothesized to be more abundant. Laboratory experiments (Helbert et al., 2013b) have suggested that repeated heating to Mercury's maximum daytime temperature may suppress such spectral features, but even thermally altered sulfides would have to comprise more than 75–84% by weight of an observed area to be detectable.
4. Hydroxylated silicates have not been identified in any VIRS spectra, including those from areas near polar deposits in permanently shadowed craters. However, the low SNR in the MASCS NIR detector at wavelengths near 1.4 μm and the restricted viewing geometry at high latitudes likely preclude detection of any weak absorption features associated with such minerals.

Acknowledgments

The MESSENGER mission is supported by the NASA Discovery Program under contract NAS5-97271 to The Johns Hopkins University Applied Physics Laboratory and NASW-00002 to the Carnegie Institution of Washington. Also providing support for this work were NASA grants NNX09AQ43G, NNX11AQ47G, NNX12AQ73G, and the MESSENGER Participating Scientist Program through grant NNX08AN29G. We thank Dan Nolet, Gerald Fine, and Jennifer Blank for synthesizing and sharing the synthetic glasses used in this study, and we thank Ed Cloutis and Paul Lucey for constructive reviews of an earlier version of this paper. This work made use of spectral data from the Keck/NASA RELAB data base at Brown University. RELAB is supported by NASA as a multi-user spectroscopy facility.

References

Blewett, D.T. et al., 2009. Multispectral images of Mercury from the first MESSENGER flyby: Analysis of global and regional color trends. Earth Planet. Sci. Lett. 285, 272–282. http://dx.doi.org/10.1016/j.epsl.2009.02.021.
Blewett, D.T. et al., 2011. Hollows on Mercury: MESSENGER evidence for geologically recent volatile-related activity. Science 333, 1856–1859. http://dx.doi.org/10.1126/science.1211681.
Blewett, D.T. et al., 2013. Mercury's hollows: Constraints on formation and composition from analysis of geological setting and spectral reflectance. J. Geophys. Res. Planets 118, 1013–1032. http://dx.doi.org/10.1029/2012JE004174.
Burbine, T.H., McCoy, T.J., Nittler, L.R., Benedix, G.K., Cloutis, E.A., Dickinson, T.L., 2002. Spectra of extremely reduced assemblages: Implications for Mercury. Meteorit. Planet. Sci. 37, 1233–1244.
Burns, R.G., 1993. Mineralogical Applications of Crystal Field Theory, second ed. Cambridge University Press, Cambridge, 551pp.
Chabot, N.L. et al., 2012. Areas of permanent shadow in Mercury's south polar region ascertained by MESSENGER orbital imaging. Geophys. Res. Lett. 39, L09204. http://dx.doi.org/10.1029/2012GL051526.
Cintala, M.J., 1992. Impact-induced thermal effects in the lunar and mercurian regoliths. J. Geophys. Res. 97, 947–973. http://dx.doi.org/10.1029/91JE02207.
Cloutis, E.A., McCormack, K.A., Bell, J.F., Hendrix, A.R., Bailey, D.T., Craig, M.A., Mertzman, S.A., Robinson, M.S., Riner, M.A., 2008. Ultraviolet spectral reflectance properties of common planetary minerals. Icarus 197, 321–347.
Denevi, B.W. et al., 2009. The evolution of Mercury's crust: A global perspective from MESSENGER. Science 324, 613–618. http://dx.doi.org/10.1126/science.1172226.
Denevi, B.W. et al., 2013. The distribution and origin of smooth plains on Mercury. J. Geophys. Res. Planets 118, 891–907. http://dx.doi.org/10.1002/jgre.20075.
Evans, L.G. et al., 2012. Major-element abundances on the surface of Mercury: Results from the MESSENGER Gamma-Ray Spectrometer. J. Geophys. Res. 117, E00L07. http://dx.doi.org/10.1029/2012JE004178.
Everitt, B.S., Landau, S., Leese, M., Stahl, D., 2011. Cluster Analysis, fifth ed. John Wiley, London, 346pp.
Goudge, T.A. et al., 2012. Global inventory and characterization of pyroclastic deposits on Mercury: New insights into pyroclastic activity from MESSENGER orbital data. Lunar Planet. Sci. 43. Abstract 1659.
Greenspon, A.S., Hibbitts, C.A., Dyar, M.D., 2012. Compositional dependencies in ultraviolet reflectance spectra of synthetic glasses relevant to airless bodies. Lunar Planet. Sci. 43. Abstract 2490.
Hapke, B., 2001. Space weathering from Mercury to the asteroid belt. J. Geophys. Res. 106, 10039–10073. http://dx.doi.org/10.1029/2000JE001338.
Hapke, B., 2012. Theory of Reflectance and Emittance Spectroscopy, second ed. Cambridge University Press, New York, 528pp.
Harmon, J.K., Slade, M.A., Rice, M.S., 2011. Radar imagery of Mercury's putative polar ice: 1999–2005 Arecibo results. Icarus 211, 37–50.
Hawkins III, S.E. et al., 2007. The Mercury Dual Imaging System on the MESSENGER spacecraft. Space Sci. Rev. 131, 247–338.
Head, J.W. et al., 2008. Volcanism on Mercury: Evidence from the first MESSENGER flyby. Science 321, 69–72. http://dx.doi.org/10.1126/science.1159256.
Head, J.W. et al., 2011. Flood volcanism in the northern high latitudes of Mercury revealed by MESSENGER. Science 333, 1853–1856. http://dx.doi.org/10.1126/science.1211997.

Helbert, J., Maturilli, A., 2009. The emissivity of a fine-grained labradorite sample at typical Mercury dayside temperatures. Earth Planet. Sci. Lett. 285, 347–354. http://dx.doi.org/10.1016/j.epsl.2009.02.031.

Helbert, H. et al., 2013a. A comparison of the spectral properties on the Caloris and Rembrandt impact basins. Lunar Planet. Sci. 44. Abstract 1496.

Helbert, J., Maturilli, A., D'Amore, M., 2013b. Visual and near-infrared reflectance spectra of thermally processed synthetic sulfides as a potential analog for the hollow forming materials on Mercury. Earth Planet. Sci. Lett. 369–370, 233–238. http://dx.doi.org/10.1016/j.epsl.2013.03.045.

Hillier, J., Buratti, B., Hill, K., 1999. Multispectral photometry of the Moon and absolute calibration of the Clementine UV/VIS camera. Icarus 141, 205–225.

Hinrichs, J.L., Lucey, P.G., 2002. Temperature-dependent near-infrared spectral properties of minerals, meteorites, and lunar soil. Icarus 155, 169–180. http://dx.doi.org/10.1006/icar.2001.6754.

Holsclaw, G.M., McClintock, W.E., Domingue, D.L., Izenberg, N.R., Blewett, D.T., Sprague, A.L., 2010. A comparison of the ultraviolet to near-infrared spectral properties of Mercury and the Moon as observed by MESSENGER. Icarus 209, 179–194. http://dx.doi.org/10.1016/j.icarus.2010.05.001.

Izenberg, N.R. et al., 2012. Laboratory measurements: Spectral reflectance of planetary-analog materials under relevant conditions. Paper PS06-A003, presented at the Asia Oceania Geosciences Society – American Geophysical Union (Western Pacific Geophysics Meeting) Joint Assembly, Singapore. <http://www.asiaoceania.org/aogs2012/mars2/timetable.asp> (13–17.08.12).

Izenberg, N.R., Wieder, S.Z., Nittler, L.R., Solomon, S.C., 2013. Correlating reflectance and X-ray spectroscopic data from MESSENGER. Lunar Planet. Sci. 44. Abstract 3018.

Kerber, L., Head, J.W., Solomon, S.C., Murchie, S.L., Blewett, D.T., Wilson, L., 2009. Explosive volcanic eruptions on Mercury: Eruption conditions, magma volatile content, and implications for mantle volatile abundances. Earth Planet. Sci. Lett. 285, 263–271. http://dx.doi.org/10.1016/j.epsl.2009.04.037.

Kerber, L. et al., 2011. The global distribution of pyroclastic deposits on Mercury: The view from MESSENGER flybys 1–3. Planet. Space Sci. 59, 1895–1909. http://dx.doi.org/10.1016/j.bbr.2011.03.031.

Klima, R.L., Pieters, C.M., Dyar, M.D., 2007. Spectroscopy of synthetic Mg–Fe pyroxenes I: Spin-allowed and spin-forbidden crystal field bands in the visible and near-infrared. Meteorit. Planet. Sci. 42, 235–253.

Klima, R.L., Dyar, M.D., Pieters, C.M., 2011. Near-infrared spectra of clinopyroxenes: Effects of calcium content and crystal structure. Meteorit. Planet. Sci. 42, 235–253.

Lawrence, D.J. et al., 2013. Evidence for water ice near Mercury's north pole from MESSENGER Neutron Spectrometer measurements. Science 339, 292–296. http://dx.doi.org/10.1126/science.1229953.

Le Maitre, R.W. et al., 2005. Igneous Rocks: A Classification and Glossary of Terms, Recommendations of the International Union of Geological Sciences, Subcommission on the Systematics of Igneous Rocks, second ed. Cambridge University Press, Cambridge, 256pp.

Lucey, P.G., Noble, S.K., 2008. Experimental test of a radiative transfer model of the optical effects of space weathering. Icarus 197, 348–353.

Lucey, P.G., Riner, M.A., 2011. The optical effects of small iron particles that darken but do not redden. Icarus 212, 451–462. http://dx.doi.org/10.1016/j.icarus.2011.01.022.

Matson, D.L., Johnson, T.V., Veeder, G., 1977. Soil maturity and planetary regoliths – The Moon, Mercury, and the asteroids. Proc. Lunar Science Conf. 8, 1001–1011.

McClintock, W.E., Lankton, M.R., 2007. The Mercury Atmospheric and Surface Composition Spectrometer for the MESSENGER mission. Space Sci. Rev. 131, 481–522.

McClintock, W.E. et al., 2008. Spectroscopic observations of Mercury's surface reflectance during MESSENGER's first Mercury flyby. Science 321, 62–65. http://dx.doi.org/10.1126/science.1159933.

McCubbin, F.M., Riner, M.A., Vander Kaaden, K.E., Burkemper, L.K., 2012. Is Mercury a volatile rich planet? Geophys. Res. Lett. 39, L09202. http://dx.doi.org/10.1029/2012GL051711.

Michaud, P., 1997. Clustering techniques. Future Generat. Comput. Syst. 13, 135–147. http://dx.doi.org/10.1016/S0167-739X(97)00017-4.

Mustard, J.F., Pieters, C.M., 1989. Photometric phase functions of common geologic minerals and applications to quantitative analysis of mineral mixture reflectance spectra. J. Geophys. Res. 94, 13619–13634.

Nash, D.B., Fanale, F.P., Nelson, R.M., 1980. SO_2 frost: UV–visible reflectivity and Io surface coverage. Geophys. Res. Lett. 7, 665–668. http://dx.doi.org/10.1029/GL007i009p00665.

Neumann, G.A. et al., 2013. Bright and dark polar deposits on Mercury: Evidence for surface volatiles. Science 339, 296–300. http://dx.doi.org/10.1126/science.1229764.

Nittler, L.R. et al., 2011. The major-element composition of Mercury's surface from MESSENGER X-ray spectrometry. Science 333, 1847–1850. http://dx.doi.org/10.1126/science.1211567.

Noble, S.K., Pieters, C.M., 2003. Space weathering on Mercury: Implications for remote sensing. Solar Syst. Res. 37, 31–35.

Noble, S.K., Pieters, C.M., Keller, L.M., 2007. An experimental approach to understanding the optical effects of space weathering. Icarus 192, 629–642.

Paige, D.A. et al., 2013. Thermal stability of volatiles in the north polar region of Mercury. Science 339, 300–303. http://dx.doi.org/10.1126/science.1231106.

Pieters, C.M., 1983. Strength of mineral absorption features in the transmitted component of near-infrared reflected light: First results from RELAB. J. Geophys. Res. 88, 9534–9544. http://dx.doi.org/10.1029/JB088iB11p09534.

Pieters, C.M. et al., 2000. Space weathering on airless bodies: Resolving a mystery with lunar samples. Meteorit. Planet. Sci. 25, 1101–1107. http://dx.doi.org/10.1111/j.1945-5100.2000.tb01496.x.

Pieters, C.M. et al., 2009. Character and spatial distribution of OH/H_2O on the surface of the Moon seen by M3 on Chandrayaan-1. Science 326, 568–572. http://dx.doi.org/10.1126/science.1178658.

Riner, M.A., Lucey, P.G., 2012. Spectral effects of space weathering on Mercury: The role of composition and environment. Geophys. Res. Lett. 39, L12201. http://dx.doi.org/10.1029/2012GL052065.

Riner, M.A., McCubbin, F.M., Lucey, P.G., Taylor, G.J., Gillis-Davis, J.J., 2010. Mercury surface composition: Integrating petrologic modeling and remote sensing data to place constraints on FeO abundance. Icarus 209, 301–313. http://dx.doi.org/10.1016/j.icarus.2010.05.018.

Robinson, M.S., Lucey, P.G., 1997. Recalibrated Mariner 10 color mosaics: Implications for mercurian volcanism. Science 275, 197–200.

Robinson, M.S. et al., 2008. Reflectance and color variations on Mercury: Regolith processes and compositional heterogeneity. Science 321, 66–69. http://dx.doi.org/10.1126/science.1160080.

Slade, M.A., Butler, B.J., Muhleman, D.O., 1992. Mercury radar imaging: Evidence for polar ice. Science 258, 635–640. http://dx.doi.org/10.1126/science.258.5082.635.

Solomon, S.C., McNutt Jr., R.L., Gold, R.E., Domingue, D.L., 2007. MESSENGER mission overview. Space Sci. Rev. 131, 3–39.

Sprague, A.L., Emery, J.P., Donaldson, K.L., Russell, R.W., Lynch, D.K., Mazuk, A.L., 2002. Mercury: Mid-infrared (3–13.5 μm) observations show heterogeneous composition, presence of intermediate and basic soil types, and pyroxene. Meteorit. Planet. Sci. 37, 1255–1268.

Thibault, C., Mickelson, M.E., Vilas, F., 1997. Reflectance spectroscopy of phyllosilicates from 0.4 to 1.0 μm. Bull. Am. Astron. Soc. 29, 975. Abstract 07.16-P.

Thuillier, G. et al., 2003. The solar spectral irradiance from 200 to 2400 nm as measured by the SOLSPEC spectrometer from the ATLAS and EURECA missions. Solar Phys. 214, 1–22.

Vasavada, A.R., Paige, D.A., Wood, S.E., 1999. Near-surface temperatures on Mercury and the Moon and the stability of polar ice deposits. Icarus 141, 179–193. http://dx.doi.org/10.1006/icar.1999.6175.

Vilas, F., 1985. Mercury: Absence of crystalline Fe^{2+} in the regolith. Icarus 64, 133–138.

Vilas, F., 1988. Surface composition of Mercury from reflectance spectrophotometry. In: Vilas, F., Chapman, C.R., Matthews, M.S. (Eds.), Mercury. University of Arizona Press, Tucson, Ariz., pp. 59–76.

Vilas, F., Sykes, M.V., 1996. Are low-albedo asteroids thermally metamorphosed? Icarus 124, 483–489.

Vilas, F., Jarvis, K.S., Gaffey, M.E., 1994. Iron alteration minerals in the visible and near-infrared spectra of low-albedo asteroids. Icarus 109, 274–283.

Vilas, F., Domingue, D.L., Jensen, E.A., McFadden, L.A., Coombs, C.R., Mendell, W.W., 1999. Aqueous alteration on the Moon. Lunar Planet. Sci. 30. Abstract 1343.

Vilas, F., Lederer, S.M., Gill, S.L., Jarvis, K.S., Thomas-Osip, J.E., 2006. Aqueous alteration affecting the irregular outer planets satellites: Evidence from spectral reflectance. Icarus 180, 453–463.

Vilas, F., Jensen, E.A., Domingue, D.L., McFadden, L.A., Runyon, C.J., Mendell, W.W., 2008. A newly-identified spectral reflectance signature near the lunar south pole and the South Pole-Aitken basin. Earth Planets Space 60, 67–74.

Warell, J., 2003. Properties of the hermean regolith: III. Disk-resolved vis–NIR reflectance spectra and implications for the abundance of iron. Icarus 161, 199–222. http://dx.doi.org/10.1016/S0019-1035(02)00055-6.

Warell, J., Sprague, A.L., Emery, J.P., Kozlowski, R.W.H., Long, A., 2006. The 0.7–5.3 μm IR spectra of Mercury and the Moon: Evidence for high-Ca clinopyroxene on Mercury. Icarus 180, 281–291. http://dx.doi.org/10.1016/j.icarus.2005.09.007.

Weider, S.Z. et al., 2012. Chemical heterogeneity on Mercury's surface revealed by the MESSENGER X-Ray Spectrometer. J. Geophys. Res. 117, E00L05. http://dx.doi.org/10.1029/2012JE004.

Weider, S.Z., Nittler, L.R., Starr, R.D., Solomon, S.C., 2013. The distribution of iron on the surface of Mercury from MESSENGER X-Ray Spectrometer measurements. Lunar Planet. Sci. 44. Abstract 2189.